# COMPUTATIONAL MODELING OF CONCRETE MATERIALS - STIFFNESS DEGRADATION OF CONCRETE DUE TO ASR: A COMPUTATIONAL HOMOGENIZATION APPROACH

Thuc Nhu Nguyen, R. Emre Erkmen, Leandro F.M. Sanchez, and Jianchun Li

**Biography: Thuc Nhu Nguyen** is a PhD student in the School of Civil and Environmental Engineering at University of Technology Sydney, NSW Australia. His research interests include alkali-aggregate reactions (AAR) in concrete material and reinforced concrete structures.

**R. Emre Erkmen** is an Assistant Professor in the Department of Building, Civil and Environmental Engineering at Concordia University, Montreal, Canada. His field of research is computational mechanics with applications to problems of solid mechanics.

ACI member **Leandro F. M. Sanchez** is an Assistant Professor in the Department of Civil Engineering at the University of Ottawa, Ottawa, ON, Canada. He is a member of ACI Committees 201, Durability of Concrete, 211, Proportioning Concrete Mixtures, 221, Aggregates and 555, Recycled Concrete Aggregates. His research interests include concrete durability, assessment, and rehabilitation of aging civil infrastructure.

**Jianchun Li** is a Full Professor in the School of Civil and Environmental Engineering at University of Technology Sydney, NSW Australia. His research interests include smart materials and smart structures, structural control for civil engineering, damage detection, structural health monitoring, non-destructive testing and structure rehabilitation.

## ABSTRACT

Alkali-silica reaction (ASR) is one of the most harmful distress mechanisms affecting concrete infrastructure worldwide. ASR is a chemical reaction that generates a secondary product, which induces expansive pressure within the reacting aggregate material and adjacent cement paste upon moisture uptake, leading to cracking, loss of material's integrity and functionality of the affected structure. In this work, a computational homogenization approach is proposed to model the impact of ASR-induced cracking on concrete stiffness as a function of its development. A Representative Volume Element (RVE) of the material at the mesoscale is developed which enables the input of the cracking pattern and extent observed from a series of experimental testing. The model is appraised on concrete mixtures presenting different mechanical properties and incorporating reactive coarse aggregates. The results have been compared with experimental results reported in literature. The case studies considered for the analysis show that stiffness reduction of ASR-affected concrete presenting distinct damage degrees can be captured by using the proposed meso-scale model as the predictions of the proposed methodology fall in between upper and lower bounds of the experimental results.



**Keywords:** Alkali-Silica Reaction; Crack configuration; Computational Homogenization; Representative Volume Element.


## INTRODUCTION

Alkali-silica reaction (ASR) is one of the most harmful distress mechanisms affecting the serviceability and durability of concrete infrastructure worldwide. ASR is a chemical reaction between the alkalis (i.e. $Na^+$, $K^+$ and $OH^-$) from the concrete pore solution and some reactive mineral phases present in the aggregates used to make concrete. This reaction generates a secondary product, the so-called ASR gel, that swells under moisture uptake, leading to important crack formation followed by reductions in mechanical properties[1-3]. Several approaches, recommendations, and test procedures, have been developed to assess the potential alkali-reactivity of concrete aggregates and the efficiency of preventive measures (e.g. control of the cement & concrete alkali content, use of supplementary cementing materials (SCMs), use of lithium based admixtures, etc.) before their use in the field[4, 5, 6, 7, 8]. Despite a few issues with some of these test procedures and the constant need of improvement in the different standards/protocols, the majority of experts agree that in general, it is now possible to build new concrete infrastructure with limited risk of ASR. However, there is currently no consensus about the most efficient method(s) that should be implemented, and when, for the rehabilitation of ASR-affected concrete infrastructure[4, 6, 9, 10, 11]. In this context, numerical models might be necessary, enabling further analysis of ASR structural implications and ensuring a better decision making. Pietruszczak[12], Saouma[13], Erkmen et al.[14] and Gorga et al.[15] employed phenomenological elasto-plastic and damage models to consider ASR effect on structural behaviour by degrading concrete properties. However, to fully understand ASR-induced expansion and damage development, its distress mechanism needs to be identified. Reinhardt and Mielich[16] proposed two different mechanisms for ASR damage in concrete: (1) ASR gel formation at the aggregate particles/interfacial transition zone (ITZ), thus inducing swelling and cracking in the cement paste; and (2) cracks generation within the aggregate particles due to gel pockets formation, which propagates to the cement paste as the expansion level increases. The former mechanism has been adopted in several ASR numerical models such as in Multon[17], Poyet[18], Suwito[19] and Nielsen[20]; yet, other researchers, such as Dunant and Scrivener[21] claimed the former approach to be incomplete and adopted the latter mechanism for numerical simulations.

The development of cracks within the aggregate particles at the early stages of the chemical reaction has been confirmed by a series of microscopic analyses from Sanchez[22, 23]. Sanchez[22, 23] evaluated a wide number of concrete mixtures incorporating over ten distinct reactive aggregate particles through the *Damage Rating Index (DRI)* method. The DRI is a petrographic protocol performed with the use of a stereomicroscope (approximately 15-16x magnification) where damage features generally associated with ASR are counted through a 1 $cm^2$ (0.155 $in^2$) grid drawn on the surface of polished concrete sections[22].

In order to capture the distress and damage development mechanisms due to ASR, Comby-Peyrot[24], Dunant and Scrivener[21], Cusatis et al[25], Ishakov et al[26], and Rezaghani et al[27] used meso-scale modeling. Meso-scale models generally introduce the aggregates and the cement paste explicitly; thus, concrete is modelled as a heterogeneous material with the aim of better understanding the effects of composite interactions and local damage mechanisms. Based on experimental observations, Sanchez[23] proposed a qualitative description of ASR induced crack generation and propagation as a function of its induced expansion development. A meso-scale computational model is required for the concrete material to adopt the model developed by Sanchez[23].

## RESEARCH SIGNIFICANCE

ASR is known to significantly reduce concrete stiffness. Models able to quantify the stiffness loss of ASR-affected concrete are required. This work aims at developing a meso-scale model to provide a thorough understanding of stiffness reduction as a function of ASR induced crack development. The crack pattern and extent from experimental observations are explicitly and efficiently introduced into the meso-scale model using the Extended Finite Element Method. A first-order computational homogenization procedure is developed to determine the effective stiffness. The outcomes of the proposed model are compared with experimental results; evaluation on its accuracy to describe ASR-distress development is performed.

## COMPUTATIONAL HOMOGENIZATION APPROACH

### Equilibrium of a deformable body

Let $\sigma_{ij}$ denote the stress tensor and $u_i$ be the displacement vector field, $\mathbf{u} = \langle u_1 \quad u_2 \rangle^{\mathrm{T}}$. The stress tensor $\boldsymbol{\sigma}$ is related to the displacement gradient through the constitutive relation, i.e.

$$\boldsymbol{\sigma} = \mathbf{D} : \nabla_{\mathbf{x}} \otimes \mathbf{u} \tag{1}$$

in which components of the stiffness matrix $\mathbf{D}$, in general, are functions of the location vector $\mathbf{x} = \langle x_1 \quad x_2 \rangle^{\mathrm{T}}$ in a heterogeneous continuum, $\nabla_{\mathbf{x}}$ is the gradient operator, i.e., $\nabla_{\mathbf{x}}^{\mathrm{T}} = \langle \partial/\partial x_1 \quad \partial/\partial x_2 \rangle$, ':' is the double dot product and '$\otimes$' is the tensorial product . The stress field is continuous (can be weakly continuous between elements after discretization). The displacement field is continuous within the bulk of the material and can become discontinuous between the interfaces. We limit our analysis to 2D problems, and the stiffness matrix for the bulk of the continuum has generally six independent components considering the symmetry of the shear stresses $\sigma_{12} = \sigma_{21}$, i.e.,

$$\mathbf{D} = \begin{bmatrix} D_{1111} & D_{1122} & D_{1112} \\ D_{1122} & D_{2222} & D_{2212} \\ D_{1112} & D_{2212} & D_{1212} \end{bmatrix} \tag{2}$$

The equilibrium equations can be written as

$$\nabla_{\mathbf{x}} \cdot \boldsymbol{\sigma} + \mathbf{p} = 0 \qquad \text{in} \qquad \Omega \tag{3}$$

$$\mathbf{u} = \mathbf{r} \qquad \text{in} \qquad \Gamma_D \tag{4}$$

$$\mathbf{n} \cdot \boldsymbol{\sigma} = -\mathbf{s} \qquad \text{in} \qquad \Gamma_N \tag{5}$$

where $\Omega$ , $\Gamma_D$ and $\Gamma_N$ are the analysis domain, Dirichlet and Neumann boundaries respectively, '.' is the dot product, **p** is the body force vector and **n** is the normal vector component to the boundary surface. Dirichlet and Neumann boundaries are non-overlapping and decompose the whole external boundary, i.e., $\partial\Omega = \Gamma$ where $\Gamma = \Gamma_D \cup \Gamma_N$ and $\Gamma_D \cap \Gamma_N = \varnothing$ . The body force per unit volume in the analysis domain is denoted with $p_i$, the specified displacement at the Dirichlet boundary is **r** and the specified traction at the Neumann boundary is **s**. The Galerkin weak form of the above governing equations from Eqs. (3) to (5) can be expressed after integration by parts as

$$\int_{\Omega} \nabla_{\mathbf{x}} \otimes \delta\mathbf{u} : \boldsymbol{\sigma}\, d\Omega + \int_{\Omega} \delta\mathbf{u} \cdot \mathbf{p}\, d\Omega + \int_{\Gamma_N} \delta\mathbf{u} \cdot \mathbf{s}\, d\Gamma = 0 \tag{6}$$

where the admissible displacement field $\mathbf{u}$ is prescribed at the boundary $\Gamma_D$ as in Eq. (4) and therefore, its variation vanishes, i.e., $\delta\mathbf{u} = \mathbf{0}$ in $\Gamma_D$.

## Homogenization

**Separation of scales and first-order homogenization:** In the description of our problem, the assumption is that heterogeneous medium has rapidly oscillating properties and the sizes of the heterogeneities are small compared to the overall size of the medium. Our aim is to compute the macro-scale effective stiffness properties from the known meso-scale properties which represent an average and thus, the small-scale variations will not be present in the homogenized problem, i.e.,

$$\hat{\mathbf{D}} : \nabla \otimes \nabla \otimes \overline{\mathbf{u}} = -\mathbf{p} \qquad \text{in} \qquad \Omega \tag{7}$$

where $\hat{\mathbf{D}}$ is the effective stiffness matrix after homogenization. In order to capture the meso-scale influence on the effective stiffness, a scaling parameter $\eta \ll 1$ is introduced which represents the ratio between the size of the meso-scale structure and the macro-structure and thus, the stiffness is assumed to be varying based on this small parameter[28]. Analytically, the homogenized stiffness $\hat{\mathbf{D}}$ is defined as the case when $\eta \to 0$. Therefore, the size of the heterogeneity is introduced as a variable to be able to describe the homogenous case as a special case (see **Fig. 1**).

The displacement field $\overline{\mathbf{u}}$ in Eq. (7) is called the first approximate solution. The idea is to approximate the solution of the heterogeneous problem by using the solution of a simpler problem, which is the homogenous problem. Thus, $\overline{\mathbf{u}}$ refers to the solution of a simpler homogenized problem and the complete displacement field $\mathbf{u}$ is represented in the form of asymptotic expansion as

$$\mathbf{u}(\mathbf{x},\mathbf{y}) = \overline{\mathbf{u}}(\mathbf{x},\mathbf{y}) + \eta\overline{\overline{\mathbf{u}}}(\mathbf{x},\mathbf{y}) + \eta^2\overline{\overline{\overline{\mathbf{u}}}}(\mathbf{x},\mathbf{y}) + \ldots \tag{8}$$

The oscillatory behaviour is due to heterogeneity and therefore, meso-scale oscillations are due to the higher-order contributions, i.e. $\bar{\bar{\mathbf{u}}}, \bar{\bar{\bar{\mathbf{u}}}},\ldots$. Due to different orders of $\eta$, that form of approximation in Eq. (8) introduces a hierarchy between the contributions of each term in the series. In order to make the position vector $\mathbf{x}$ independent of the scaling parameter $\eta$ and thus, to construct globally valid solutions for a variable $\eta$, two spatial scales are incorporated into the problem. This allows $\mathbf{x}$ always refer to the same material point as $\eta$ changes and the position vector $\mathbf{x}$ now has the meaning of the slow scale or the macro-scale coordinate, measuring variations within the global region of interest only. Therefore, in Eq. (8) there is another vector $\mathbf{y} = \mathbf{x}/\eta$ which is the fast coordinate, measuring variations within one period cell. As a result, the derivative operations transform into[28]

$$\frac{\partial}{\partial \mathbf{x}} \to \frac{\partial}{\partial \mathbf{x}} + \frac{1}{\eta}\frac{\partial}{\partial \mathbf{y}} \tag{9}$$

Thus, the analysis domain of the problem is extended as $\Omega^{\eta} = \Omega \times \eta \mathrm{Y}$, where Y denotes the domain of one cell that periodically repeats. In this case, Eq. (3) takes the form

$$\nabla_{\mathbf{x}} \cdot \boldsymbol{\sigma}(\mathbf{x},\mathbf{y}) + \frac{1}{\eta}\nabla_{\mathbf{y}} \cdot \boldsymbol{\sigma}(\mathbf{x},\mathbf{y}) = -\mathbf{p}(\mathbf{x}) \tag{10}$$

Where the asymptotic expansion of the stress tensor can be written as

$$\boldsymbol{\sigma}(\mathbf{x},\mathbf{y}) = \tilde{\boldsymbol{\sigma}}(\mathbf{x},\mathbf{y}) + \eta\tilde{\tilde{\boldsymbol{\sigma}}}(\mathbf{x},\mathbf{y}) + \eta^2\tilde{\tilde{\tilde{\boldsymbol{\sigma}}}}(\mathbf{x},\mathbf{y}) + \ldots \tag{11}$$

By substituting Eq. (8) into Eq. (1) and using derivative transform in Eq. (9), one obtains

$$\breve{\boldsymbol{\sigma}}_{ij}(\mathbf{x},\mathbf{y}) = \mathbf{D}(\mathbf{x},\mathbf{y}) : \nabla \otimes \bar{\mathbf{u}}(\mathbf{x}) \tag{12}$$

$$\tilde{\boldsymbol{\sigma}}(\mathbf{x},\mathbf{y}) = \mathbf{D}(\mathbf{x},\mathbf{y}) : \left(\nabla \otimes \bar{\mathbf{u}}_k(\mathbf{x}) + \nabla \otimes \bar{\bar{\mathbf{u}}}(\mathbf{x})\right) = \bar{\boldsymbol{\sigma}}(\mathbf{x},\mathbf{y}) + \bar{\bar{\boldsymbol{\sigma}}}(\mathbf{x},\mathbf{y}) \tag{13}$$

$$\tilde{\tilde{\boldsymbol{\sigma}}}(\mathbf{x},\mathbf{y}) = \mathbf{D}(\mathbf{x},\mathbf{y}) : \left(\nabla \otimes \bar{\bar{\mathbf{u}}}(\mathbf{x},\mathbf{y}) + \nabla \otimes \bar{\bar{\bar{\mathbf{u}}}}(\mathbf{x},\mathbf{y})\right) \tag{14}$$

Because of the fact that the series in Eq. (11) does not contain the term $\eta^{-1}\breve{\boldsymbol{\sigma}}(\mathbf{x},\mathbf{y})$, Eq. (12) should vanish. This is because $\eta^{-1}$ is not bounded as $\eta \to 0$ which is contrary to the periodicity assumption for $\boldsymbol{\sigma}(\mathbf{x},\mathbf{y})$. Thus, from Eq. (12) it can be concluded that $\bar{\mathbf{u}}$ cannot depend on the fast coordinate $\mathbf{y}$, i.e., $\bar{\mathbf{u}} = \bar{\mathbf{u}}(\mathbf{x})$. In the following analysis, only the first non-vanishing stress term is used, i.e., $\boldsymbol{\sigma}(\mathbf{x},\mathbf{y}) = \tilde{\boldsymbol{\sigma}}(\mathbf{x},\mathbf{y})$ and consequently, the terms higher than first order in the displacement ansatz are neglected, i.e., $\tilde{\tilde{\boldsymbol{\sigma}}}(\mathbf{x},\mathbf{y})=0$ and $\mathbf{u}(\mathbf{x},\mathbf{y}) = \bar{\mathbf{u}}(\mathbf{x}) + \eta\bar{\bar{\mathbf{u}}}(\mathbf{x},\mathbf{y})$. Note that $\bar{\bar{\mathbf{u}}}(\mathbf{x},\mathbf{y})$ is a periodic function in Y, i.e. $\bar{\bar{\mathbf{u}}}(\mathbf{x},\mathbf{y})=\bar{\bar{\mathbf{u}}}(\mathbf{x},\mathbf{y}+\mathbf{Y})$, where $\mathbf{Y}$ is the period in fast coordinate (**Fig. 1**). Substituting Eq. (13) into Eq. (10) and grouping the terms according to their order, i.e., $O(1)$ and $O(1/\eta)$ produces

$$\nabla_{\mathbf{x}} \cdot \tilde{\boldsymbol{\sigma}}(\mathbf{x},\mathbf{y}) + \mathbf{p}(\mathbf{x}) = 0 \qquad \text{in} \qquad \Omega \tag{15}$$

$$\nabla_{\mathbf{y}} \cdot \tilde{\boldsymbol{\sigma}}(\mathbf{x},\mathbf{y}) = 0 \qquad \text{in} \qquad \mathrm{Y} \tag{16}$$

**Variational setting for homogenization**: By integrating the balance in Eq. (15) over a domain of one cell and using the variation of the first approximate displacement field $\delta\bar{\mathbf{u}}$, after integration by parts the weak form of the equilibrium equation can be obtained as

$$\int_{\Omega} \nabla_{\mathbf{x}} \otimes \delta\bar{\mathbf{u}} : \hat{\boldsymbol{\sigma}}\, d\Omega + \int_{\Omega} \delta\bar{\mathbf{u}} \cdot \mathbf{p}\, d\Omega + \int_{\Gamma_N} \delta\bar{\mathbf{u}} \cdot \mathbf{s}\, d\Gamma = 0 \tag{17}$$

where $\hat{\boldsymbol{\sigma}}$ is the effective stress tensor and determined by averaging the stress tensor over one cell, i.e.

$$\hat{\boldsymbol{\sigma}} = |\mathrm{Y}|^{-1} \int_{\mathrm{Y}} \boldsymbol{\sigma}(\mathbf{x},\mathbf{y}) d\mathrm{Y} = |\mathrm{Y}|^{-1} \int_{\mathrm{Y}} \left[ \bar{\boldsymbol{\sigma}}(\mathbf{x},\mathbf{y}) + \bar{\bar{\boldsymbol{\sigma}}}(\mathbf{x},\mathbf{y}) \right] d\mathrm{Y} \tag{18}$$

where $|\mathrm{Y}| = \int_{\mathrm{Y}} d\mathrm{Y}$ is the area of the cell (i.e. volume for unit thickness). In obtaining Eq. (17), it has been assumed that the source terms $\mathbf{p}$ and $\mathbf{s}$ are independent of the fast coordinate $\mathbf{y}$. For the solution of the global equilibrium problem in Eq. (17), the whole stress tensor $\boldsymbol{\sigma}$ needs to be expressed in terms of the average displacement gradient $\nabla \otimes \bar{\mathbf{u}}$. For that purpose, Eq. (16) is used in the weak form by multiplying with the virtual displacement fluctuations $\delta\bar{\bar{\mathbf{u}}}$ and integrating over a domain of one cell **Y**. After integration by parts with respect to fast coordinate $\mathbf{y}$, one obtains

$$\int_{Y} \nabla_y \otimes \delta\overline{\overline{\mathbf{u}}} : \boldsymbol{\sigma} dY - \int_{\Psi} \delta\overline{\overline{\mathbf{u}}} \cdot \boldsymbol{\sigma} \cdot \mathbf{n}\, d\Psi = 0 \tag{19}$$

where $\Psi = \partial Y$ is the boundary of the cell and $\Psi$ represents the fast coordinate on the cell boundary. Eq. (19) is the Hill-Mandel condition for scale separation, which allows decoupling of the analysis of a heterogeneous material into analyses at the local and global levels. Thus, the solution of Eq. (19) builds the relationship between the gradients of the average displacement and the stress in one cell Y. Under the assumption of $\eta \to 0$, by using Eq. (19), the weak form over the whole domain in Eq. (6) can be replaced with Eq. (17) for the global analysis. Thus, the heterogeneous domain can be replaced by the equivalent homogenous material having calculated the effective properties at the local level. Despite the fact that $\overline{\overline{\mathbf{u}}}(\mathbf{x},\mathbf{y})$ is a periodic function, i.e., $\int_{Y} \nabla_y \otimes \overline{\overline{\mathbf{u}}}(\mathbf{x},\mathbf{y}) dY = \mathbf{0}$, the integral of the stress component $\overline{\overline{\boldsymbol{\sigma}}}$ generally does not vanish in Y, i.e., $\int_{Y} \overline{\overline{\boldsymbol{\sigma}}}(\mathbf{x},\mathbf{y}) dY = \int_{Y} \mathbf{D}(\mathbf{x},\mathbf{y}) : \nabla_y \otimes \overline{\overline{\mathbf{u}}}(\mathbf{x},\mathbf{y}) dY \neq \mathbf{0}$ thus, the two-scale analysis introduces the effect of fluctuations due to heterogeneity in the global analysis.

**RVE Boundary Value Problem**: Practically speaking, in order to solve the cell problem in Eq. (19) a Representative Volume Element (RVE) needs to be introduced. The RVE is defined as the smallest structural volume that sufficiently accurately represents the overall macroscopic stiffness properties of interest. Thus, the size of the RVE should be selected large enough to be statistically representative of the distributions of the inclusions. Because of the finite size of the RVE, i.e., $\eta \neq 0$, homogenization is approximate unless exact RVE boundary conditions are imposed. Since exact boundary conditions are not known *a-priori* a chosen RVE is generally analysed using either uniform gradient, uniform traction or periodic boundary conditions. Therefore, the information on the cell boundary is lost due to Hill-Mandel condition for scale separation as there might be many candidates for $\bar{\bar{\mathbf{u}}}$ that satisfy Eq. (19). In other words, there is a meso-scale effect due to meso-scale fluctuations at the boundary of a finite size RVE that is not resolved in the two-scale analysis. The assumed meso-scale field existing at the RVE boundary influences the effective modulus by influencing the effective stress field, e.g. in Kanit et al.[29]. We assume that the aggregate and ASR induced crack distributions are such that the whole structure consists of spatially repeated cells as indicated in **Fig. 1**. Therefore, Periodic Boundary Conditions are assumed herein and its implementation is discussed in the next section. Finite size RVE volume and boundary surface are denoted as $V_{RVE}$ and $S_{RVE}$, respectively and thus, $\lim_{|V_{RVE}|\to 0} V_{RVE} = \mathrm{Y}$ and $\lim_{|V_{RVE}|\to 0} S_{RVE} = \Psi$. In first-order homogenization, the displacement at the RVE boundary i.e., at $\boldsymbol{\psi} \in S_{RVE}$ can be imposed as

$$\mathbf{u}(\boldsymbol{\psi}) = \bar{\mathbf{u}}(\bar{\mathbf{y}}) + (\boldsymbol{\psi} - \bar{\mathbf{y}}) \cdot \mathbf{g} + \mathbf{u}'(\boldsymbol{\psi}) \tag{20}$$

where $\bar{\mathbf{y}} = |V_{RVE}|^{-1} \int_{V_{RVE}} \mathbf{y}\, \mathrm{dY}$ refers to the centre of the RVE, $\mathbf{g}$ is the specified average displacement gradient field obtained from the global problem in Eq. (17) i.e., $\mathbf{g} = \nabla_{\mathbf{x}} \otimes \bar{\mathbf{u}}$, and $\lim_{|V_{RVE}|\to 0} \mathbf{u}'(\boldsymbol{\psi}) = \eta \bar{\bar{\mathbf{u}}}(\boldsymbol{\psi})$ is the contribution of the meso-scale fluctuations at the boundary which is generally unknown. It should be noted that for convenience and without losing generality, for the purpose of determining the local stress field, the origin of the RVE coordinates can be taken at $\bar{\mathbf{y}}$, i.e., $\bar{\mathbf{y}} = 0$ and the average displacement can be assumed zero, i.e., $\bar{\mathbf{u}}(\bar{\mathbf{y}}) = 0$.
By considering that the forcing term for the deformation of the RVE is the constant average displacement gradient one obtains

$$\int_{S_{RVE}} \mathbf{u} \otimes \mathbf{n}\, \mathrm{d}\Psi = \mathbf{g} \int_{V_{RVE}} \mathrm{dY} \tag{21}$$

By introducing $\delta\boldsymbol{\sigma}$ as the weighting function in the weak form of Eq. (21), one obtains the RVE problem similar to the general form introduced in Miehe and Koch[30] based on the Lagrange multiplier technique[31], i.e.

$$\int_{V_{RVE}} \nabla_{\mathrm{y}} \otimes \delta\bar{\bar{\mathbf{u}}} : \boldsymbol{\sigma}\,\mathrm{dY} - \int_{S_{RVE}} \delta\bar{\bar{\mathbf{u}}} \cdot \boldsymbol{\lambda}\,\mathrm{d}\Psi - \int_{S_{RVE}} \delta\boldsymbol{\lambda} \cdot \left(\mathbf{u} - \boldsymbol{\psi} \cdot \mathbf{g}\right) \mathrm{d}\Psi = 0 \tag{22}$$

where $\int_{V_{RVE}} \mathrm{dY} = \int_{S_{RVE}} \boldsymbol{\psi} \cdot \mathbf{n}\,\mathrm{d}\Psi$ has been used and $\boldsymbol{\lambda} = \mathbf{n} \cdot \boldsymbol{\sigma}$ is the Lagrange multiplier vector which constraints the average displacement in the RVE based on the specified average displacement gradient field $\mathbf{g}$. Thus, each of the two components of $\boldsymbol{\lambda}$ can be identified as the total tractions at the boundary points $\boldsymbol{\psi} \in S_{RVE}$. Eq. (22) can be solved to determine the whole stress field $\boldsymbol{\sigma}$ in terms of the average displacement gradient $\mathbf{g}$. From the solution of Eq. (22) and by using Eq. (18), one obtains the relationship

$$\hat{\boldsymbol{\sigma}} = \hat{\mathbf{D}} : \mathbf{g} \tag{23}$$

where $\hat{\mathbf{D}}$ is the effective stiffness matrix to be used for the global solution in Eq. (17). The schematic outline in **Fig. 2** describes the multi-scale analysis procedure based on the idea of separation of scales. Once the boundary conditions are chosen, equations can be solved to calculate the local RVE stress tensor $\boldsymbol{\sigma}$. Accordingly, the effective stress tensor $\hat{\boldsymbol{\sigma}}$ can be calculated by using the local stress tensor $\boldsymbol{\sigma}$ in Eq. (18). Three cases of displacement gradient need to be introduced to determine all components of the stiffness matrix through the displacement gradient and stress relationship in Eq. (23), i.e.

$$\left[\begin{array}{c:c:c} \hat{\sigma}_{11}^{1} & \hat{\sigma}_{11}^{2} & \hat{\sigma}_{11}^{3} \\ \hat{\sigma}_{22} & \hat{\sigma}_{22}^{2} & \hat{\sigma}_{22}^{3} \\ \hat{\sigma}_{12} & \hat{\sigma}_{12}^{2} & \hat{\sigma}_{12}^{3} \end{array}\right] = \begin{bmatrix} \hat{D}_{1111} & \hat{D}_{1122} & \hat{D}_{1112} \\ \hat{D}_{1122} & \hat{D}_{2222} & \hat{D}_{2212} \\ \hat{D}_{1112} & \hat{D}_{2212} & \hat{D}_{1212} \end{bmatrix} \begin{array}{c} \begin{array}{ccc} \text{Case1} & \text{Case2} & \text{Case3} \end{array} \\ \left[\begin{array}{c:c:c} 1 & 0 & 0 \\ 0 & 1 & 0 \\ 0 & 0 & 1 \end{array}\right] \end{array} \tag{24}$$

It should be noted that the resulting stiffness matrix is symmetrical.

## Numerical implementation

**Implementation of the RVE boundary conditions**: The numerical solution procedure can be developed by selecting the displacement field $\mathbf{u}$ in the form of

$$\mathbf{u} = \mathbf{A}\mathbf{a} \tag{25}$$

and the Lagrange multiplier field $\boldsymbol{\lambda}$ in the form of

$$\boldsymbol{\lambda} = \mathbf{G}\mathbf{h} \tag{26}$$

where $\mathbf{A}$ and $\mathbf{G}$ are the matrices of selected approximation functions for $\mathbf{u}$ and $\boldsymbol{\lambda}$, respectively. In Eqs. (25) and (26), $\mathbf{a}$ and $\mathbf{h}$ are the vectors of unknown parameters after discretization. It should be noted that for numerical implementation the rest of the equations refer to the algebraic forms after discretisation, thus matrices and vectors appear side by side are multiplied by dot product. By substituting Eqs. (25) and (26) into Eq. (22) one obtains the algebraic form of the RVE problem as

$$\begin{bmatrix} \mathbf{K} & \mathbf{S}^{\mathrm{T}} \\ \mathbf{S} & 0 \end{bmatrix} \begin{Bmatrix} \mathbf{a} \\ \mathbf{h} \end{Bmatrix} = \begin{Bmatrix} \mathbf{0} \\ \boldsymbol{\Theta}\mathbf{g} \end{Bmatrix} \tag{27}$$

where $\mathbf{K}$, $\mathbf{L}$ and $\boldsymbol{\Theta}$ can be identified as $\mathbf{K} = \int_{V_{RVE}} \frac{\partial \mathbf{A}}{\partial \mathbf{y}}^{\mathrm{T}} \mathbf{D} \frac{\partial \mathbf{A}}{\partial \mathbf{y}} \mathrm{d}\mathrm{Y}$ , $\mathbf{S} = \int_{S_{RVE}} \mathbf{G}^{\mathrm{T}} \mathbf{A} \mathrm{d}\Psi$ and $\boldsymbol{\Theta} = \int_{S_{RVE}} \mathbf{G}^{\mathrm{T}} \boldsymbol{\psi}^{\mathrm{T}} \mathrm{d}\Psi$ . In Eq. (27), the stress for the heterogeneous RVE domain is obtained according to Eq. (1), i.e., $\boldsymbol{\sigma} = -\mathbf{D}\frac{\partial \mathbf{A}}{\partial \mathbf{y}}\mathbf{a}$ and it was considered that in the RVE problem $\bar{\mathbf{u}}$ is specified, i.e., $\delta\mathbf{u} = \eta\delta\bar{\bar{\mathbf{u}}}$. From the general algebraic form of the RVE problem in Eq. (27) one obtains the following cases by imposing constraints on the Lagrange multiplier $\boldsymbol{\lambda}$ and/or the displacement $\mathbf{u}$ at the boundary $S_{RVE}$ . The interior points of the RVE are located at $\mathbf{y} \in \overline{V}_{RVE} - S_{RVE}$ , i.e., $\left\{\mathbf{y} : \mathbf{y} \in \overline{V}_{RVE} \text{ and } \mathbf{y} \notin S_{RVE}\right\}$ , where $\overline{V}_{RVE}$ is the closure of the RVE domain. On the other hand, for the purpose of imposing constraints, the boundary is decomposed into two parts, i.e., $S_{RVE} = S_{RVE}{}^{+} \cup S_{RVE}{}^{-}$ with outward normal $\mathbf{n}^{+} = -\mathbf{n}^{-}$ at associated points $\boldsymbol{\psi}^{+} \in S_{RVE}{}^{+}$ and $\boldsymbol{\psi}^{-} \in S_{RVE}{}^{-}$, respectively (see **Fig. 3a**). Every point on the boundary is paired with its image on the other side of the boundary. This pairing is done in a standard manner, e.g. in Larsson et al.[32]. Thus, a point $\boldsymbol{\psi}^{+} \in S_{RVE}{}^{+}$ on the right boundary finds its image $\boldsymbol{\psi}^{-} \in S_{RVE}{}^{-}$ at the left boundary with the same $y_2$ coordinate. Similarly, a point $\boldsymbol{\psi}^{+} \in S_{RVE}{}^{+}$ on the top boundary finds its image $\boldsymbol{\psi}^{-} \in S_{RVE}{}^{-}$ at the bottom boundary with the same $y_1$ coordinate as shown in **Fig. 3a**. Note that corner points have two images, i.e., in both horizontal and vertical directions.

The **K** and **S** matrices and the vector of nodal displacements **a** can be partitioned considering the interior and boundary nodes, as a result of which from Eq. (27) one obtains

$$\mathbf{Ka} = \begin{bmatrix} \mathbf{K}_{II} & \mathbf{K}_{IB} \\ \mathbf{K}_{IB}{}^{\mathrm{T}} & \mathbf{K}_{BB} \end{bmatrix} \begin{Bmatrix} \mathbf{a}_I \\ \mathbf{a}_B \end{Bmatrix} \tag{28}$$

and

$$\mathbf{Sa} = \begin{bmatrix} \mathbf{S}_I & \mathbf{S}_B \end{bmatrix} \begin{Bmatrix} \mathbf{a}_I \\ \mathbf{a}_B \end{Bmatrix} \tag{29}$$

where subscript $B$ refers to the boundary nodes and $I$ refers to the internal nodes. **Fig. 3b** shows the boundary nodes and the interior nodes separately in order to explain the implementation of the boundary constraint conditions explicitly. Note that as **S** is only defined through the boundary integral, $\mathbf{S}_I$ naturally vanishes at the internal nodes since $\mathbf{G} = \mathbf{0}$ at $\mathbf{y} \in \overline{V}_{RVE} - S_{RVE}$.

**Periodic displacement RVE boundary conditions**: The fine scale fluctuations of the displacement field at the boundary does not vanish, i.e., $\mathbf{u}'(\boldsymbol{\psi}) \neq 0$, however, it is assumed that due to periodicity the boundary fluctuations on $\boldsymbol{\psi}^{+} \in S_{RVE}{}^{+}$ are same on the opposite side $\boldsymbol{\psi}^{-} \in S_{RVE}{}^{-}$. Thus, considering that $\mathbf{u}'(\boldsymbol{\psi}^{+}) - \mathbf{u}'(\boldsymbol{\psi}^{-}) = 0$, the constraint for the periodicity condition can be introduced in the form of

$$\mathbf{u}(\boldsymbol{\psi}_k^{\ +}) - \mathbf{u}(\boldsymbol{\psi}_k^{\ -}) = \left(\boldsymbol{\psi}_k^{\ +} - \boldsymbol{\psi}_k^{\ -}\right)^{\mathrm{T}} \mathbf{g}\,, \tag{30}$$

where subscript $k$ refers to the node number on the boundary. Note that the total boundary traction is anti-period i.e.

$$\boldsymbol{\lambda}^{+} = -\boldsymbol{\lambda}^{-} \tag{31}$$

where $\boldsymbol{\lambda}^{+}$ and $\boldsymbol{\lambda}^{-}$ act on the nodes at $\boldsymbol{\psi}^{+} \in S_{RVE}^{\ +}$ and $\boldsymbol{\psi}^{-} \in S_{RVE}^{\ -}$, respectively. Using anti-periodicity of the traction, at the boundary nodes the stress can be expressed with reduced number of degrees of freedom using the $\mathbf{w}$ vector as

$$\mathbf{h} = \mathbf{P}^{\mathrm{T}} \mathbf{w}\,, \tag{32}$$

image

where $\mathbf{P} = \begin{bmatrix} 1 & 0 & \cdots & 0 & \cdots & -1 & 0 & 0 & \cdots & 0 \\ 0 & 1 & \cdots & 0 & \cdots & 0 & -1 & 0 & \cdots & 0 \\ \vdots & \vdots & \ddots & & \ddots & \vdots & \vdots & \vdots & \ddots & \\ 0 & 0 & \cdots & 1 & \cdots & 0 & 0 & 0 & \cdots & -1 \end{bmatrix}$. Note that in each row of $\mathbf{P}$ there are only two non-zero values which correspond to nodes that are images of each other. By substituting Eqs. (30) and (32) into Eq. (27) and using Eqs. (28) and (29) one obtains the solution of the RVE problem from the below algebraic equations as

$$\begin{bmatrix} \mathbf{K}_{II} & \mathbf{K}_{IB} & \mathbf{0} \\ \mathbf{K}_{IB}^{\ \mathrm{T}} & \mathbf{K}_{BB} & \mathbf{S}_B^{\ \mathrm{T}} \mathbf{P}^{\mathrm{T}} \\ \mathbf{0} & \mathbf{P}\mathbf{S}_B & \mathbf{0} \end{bmatrix} \begin{Bmatrix} \mathbf{a}_I \\ \mathbf{a}_B \\ \mathbf{w} \end{Bmatrix} = \begin{Bmatrix} \mathbf{0} \\ \mathbf{0} \\ \mathbf{P}\boldsymbol{\Theta}\mathbf{g} \end{Bmatrix} \tag{33}$$

Note that the last row in Eq. (33) can be interpreted as the imposition of the constraint in Eq. (30), i.e., $\mathbf{u}(\boldsymbol{\psi}_k^{\ +}) - \mathbf{u}(\boldsymbol{\psi}_k^{\ -}) = \mathbf{A}_{half}\left(\mathbf{a}_B^{\ +} - \mathbf{a}_B^{\ -}\right) = \left(\boldsymbol{\psi}^{+} - \boldsymbol{\psi}^{-}\right)^{\mathrm{T}} \mathbf{g} = \mathbf{A}_{half} \mathbf{P} \mathbf{a}_B = \mathbf{P} \boldsymbol{\psi}^{\mathrm{T}} \mathbf{g}$ as

$$\begin{aligned} &\int_{S_{RVE}} \delta\boldsymbol{\lambda}\left(\mathbf{u} - \boldsymbol{\psi}^{\mathrm{T}}\mathbf{g}\right) \mathrm{d}\Psi = \delta\mathbf{w}^{\mathrm{T}} \mathbf{P} \int_{S_{RVE}} \mathbf{G}^{\mathrm{T}}\left(\mathbf{A}\mathbf{a}_B - \boldsymbol{\psi}^{\mathrm{T}}\mathbf{g}\right) \mathrm{d}\Psi \\ &= \delta\mathbf{h}^{\mathrm{T}} \left[ \int_{S_{RVE}^{\ +}} \mathbf{G}^{\mathrm{T}}\left(\mathbf{A}\mathbf{a}_B^{\ +} - \boldsymbol{\psi}^{+\mathrm{T}}\mathbf{g}\right) \mathrm{d}\Psi + \int_{S_{RVE}^{\ -}} \mathbf{G}^{\mathrm{T}}\left(\mathbf{A}\mathbf{a}_B^{\ -} - \boldsymbol{\psi}^{-\mathrm{T}}\mathbf{g}\right) \mathrm{d}\Psi \right] \\ &= \delta\mathbf{h}^{\mathrm{T}} \int_{S_{RVE}^{\ +}} \mathbf{G}^{\mathrm{T}} \underbrace{\left(\mathbf{A}_{half}\mathbf{P}\mathbf{a}_B - \mathbf{P}\boldsymbol{\psi}^{\mathrm{T}}\mathbf{g}\right)}_{\text{Strong condition}} \mathrm{d}\Psi \end{aligned} \tag{34}$$

where $\mathbf{a}_b^{\,+}$ and $\mathbf{a}_b^{\,-}$ refer to the nodes at $\boldsymbol{\psi}^+ \in S_{RVE}^{\ \ +}$ and $\boldsymbol{\psi}^- \in S_{RVE}^{\ \ -}$, respectively, and $\mathbf{A}_{half}$ is obtained after partitioning $\mathbf{A}$ as $\mathbf{A}^{\mathrm{T}} = \begin{bmatrix} \mathbf{A}^{+\mathrm{T}} & \mathbf{A}^{-\mathrm{T}} \end{bmatrix}$ where $\mathbf{A}^+$ and $\mathbf{A}^-$ are related to the nodes at the relevant half of the boundary at $S_{RVE}^{\ \ +}$ and $S_{RVE}^{\ \ -}$, respectively and $\mathbf{A}_{half} = \mathbf{A}^+ = \mathbf{A}^-$.

**Interpolation of the displacement and Lagrange multiplier fields**: Following Melenk and Babuška[33] and Belytschko and Black[34], we express the displacement field in terms of a continuous and a discontinuous component, i.e.

$$\mathbf{u} = \mathbf{N}\mathbf{d} + \mathbf{H}\big|_{\Gamma_{DI}} \mathbf{N}\boldsymbol{\beta} \tag{35}$$

At the element level $\mathbf{N} = \begin{bmatrix} N_1 & 0 & N_2 & 0 & N_3 & 0 & N_4 & 0 \\ 0 & N_1 & 0 & N_2 & 0 & N_3 & 0 & N_4 \end{bmatrix}$ is the matrix of the standard finite-element shape functions, $\mathbf{d} = \langle d_{11} \quad d_{12} \quad d_{21} \quad d_{22} \quad d_{31} \quad d_{32} \quad d_{41} \quad d_{42} \rangle^{\mathrm{T}}$ is the column vector of nodal displacement values, $\mathbf{H}\big|_{\Gamma_{DI}}$ is the vector of Heaviside function at the discontinuity interface $\Gamma_{DI}$ and $\boldsymbol{\beta} = \langle \beta_{11} \quad \beta_{12} \quad \beta_{21} \quad \beta_{22} \quad \beta_{31} \quad \beta_{32} \quad \beta_{41} \quad \beta_{42} \rangle^{\mathrm{T}}$ is the vector of enriched degrees of freedom. Thus, $\mathbf{A}$ in Eq. (24) for one element can be written as $\mathbf{A} = \begin{bmatrix} \mathbf{N} & \mathbf{H}\big|_{\Gamma_{DI}} \mathbf{N} \end{bmatrix}$ and $\mathbf{a}$ consist of both standard and enriched degrees of freedom, i.e., $\mathbf{a}^{\mathrm{T}} = \langle \mathbf{d}^{\mathrm{T}} \quad \boldsymbol{\beta}^{\mathrm{T}} \rangle$. It should be noted that in the previous section the constraints related to boundary conditions are applied on the standard nodal displacements, i.e., $\mathbf{d}$ only and not on those of the enriched degrees of freedom due to displacement discontinuity at the interface. For the standard rectangular elements of the size $2a \times 2b$ as shown in **Fig. 4** below, the shape function components can be explicitly given below for convenience as $N_1 = (a - z_1)(b - z_2)/(4ab)$ , $N_2 = (a + z_1)(b - z_2)/(4ab)$ , $N_3 = (a + z_1)(b + z_2)/(4ab)$ and $N_4 = (a - z_1)(b + z_2)/(4ab)$. Note that for each element local coordinates $z_1$ and $z_2$ are used within the RVE coordinate system $\mathbf{y} \in \overline{V}_{RVE}$ in **Fig. 3**.

The displacement jump at the discontinuity interface $\Gamma_{DI}$ can be written as

$$[\lfloor \mathbf{u} \rfloor] = \mathbf{N}|_{\Gamma_{DI}} \boldsymbol{\beta} \tag{36}$$

where $\mathbf{N}|_{\Gamma_{DI}}$ is a partition of unity at the discontinuity interface $\Gamma_{DI}$ and vanishes everywhere else. In general, the stress field at the bulk of the heterogeneous continuum can be expressed in term of the nodal displacements as

$$\boldsymbol{\sigma} = \mathbf{D}\left(\mathbf{Bd} + \mathbf{H}|_{\Gamma_{DI}} \mathbf{B}\boldsymbol{\beta}\right) \tag{37}$$

where $\boldsymbol{\sigma}$ is the column vector of stress components, i.e., $\boldsymbol{\sigma} = \langle \sigma_{11} \quad \sigma_{22} \quad \sigma_{12} \rangle^{\mathrm{T}}$, $\mathbf{B}$ is a matrix of the derivatives of the shape functions. The traction vector at the discontinuity interface **t** can be written as

$$\mathbf{t} = \mathbf{c}\,\mathbf{N}|_{\Gamma_{DI}} \boldsymbol{\beta} \tag{38}$$

where **c** is a matrix of interface cohesive stiffness. Note that in Eq. (6), stress $\boldsymbol{\sigma}$ is conjugate to displacement gradient while, **t** is conjugate to displacement jump at the discontinuity interface, therefore **t** is a vector of two components in two directions. On the other hand, for the interpolation of the Lagrange multiplier field $\boldsymbol{\lambda}$ in Eq. (26) **G** is selected based on linear functions. Thus, for one element it can be written as $\mathbf{G} = \begin{bmatrix} L_1 & 0 & L_2 & 0 \\ 0 & L_1 & 0 & L_2 \end{bmatrix}$, in which $L_1 = \left(0.5l - z_b\right)/l$ and $L_2 = \left(0.5l + z_b\right)/l$. As shown in **Fig. 5**, $z_b$ refers to the one dimensional edge coordinate and $l$ is the corresponding edge span (e.g. either $l = 2a$ or $l = 2b$ in **Fig. 4**). For one element, **h** in Eq. (26) can be written as $\mathbf{h} = \langle h_1 \quad h_2 \rangle^{\mathrm{T}}$.

## MODELLING CONCRETE STIFFNESS REDUCTION DUE TO ASR

### ASR distress development and its effect on concrete stiffness properties

ASR in concrete generates a secondary product (i.e. ASR gel) that induces pressure and leads to crack formation within the aggregate particles and surrounding cement paste (**Fig. 6a**).

Sanchez[23] proposed a qualitative meso-scale model to describe ASR cracks generation and propagation as a function of its induced expansion development. According to the author, ASR cracks are initially developed within aggregate particles at low expansion levels (i.e. up to 0.05%). At moderate levels of expansion (i.e. 0.12%), although some additional cracks are still generated within the aggregates, the existing cracks previously formed at low expansion levels keep propagating and may reach the boundaries of the aggregate particles. Once the expansion increases to higher levels (i.e. > 0.2%), the overall damage is mostly dominated by the propagation of pre-existing cracks to the surrounding cement paste (**Fig. 6b)**. It is worth noting that two types of cracks may be induced by ASR in concrete: (1) cracks "cutting" the aggregate particles, namely "sharp cracks" (type A), and (2) cracks outlining the aggregate particle boundaries, namely "onion skin cracks" (type B). The proportion of onion cracks (type B) is about 20-30 % of the total cracks, yet it may vary according to the aggregate lithotype (i.e. mineralogy). In addition to the extension of cracks from reactive aggregate particles as shown in **Fig. 6b**, several cracks develop in the surrounding cement paste due to swelling pressures from the particles, yet, do not penetrate into the particle.

In the research conducted by Sanchez[23], crack density (number and length of cracks per area) has been related to the reduction of stiffness of affected concrete. **Fig. 7** illustrates Sanchez[35] results, include the changes in the measured elasticity moduli (**Fig. 7a)** and crack densities (**Fig. 7b)** corresponding to different levels of expansion reached by 35 MPa concrete specimens incorporating distinct reactive coarse aggregates. The figure shows that as the expansion level increases, the elasticity modulus reduces while the crack density increases. According to Sanchez et al.[22, 23], the proportion of open cracks in aggregate and cement paste are different for different concrete mixtures and levels of expansion. However, in all tested specimens, the majority of open cracks are found in the aggregate particles, being around 70% to 85% of the total number of cracks. More details on the experimental setup and measurements can be found in Sanchez et al.[22, 23, 35]. Note that the legends used in Fig.7 (as well as Fig. 10) refer to the type of reactive aggregate, the type of non-reactive aggregate and the concrete grade, respectively, (e.g. for "NM + Lav 35", NM is reactive coarse aggregate, Lav is non-reactive fine aggregate and 35 is the concrete grade i.e. 35 MPa). The notation is adopted from Sanchez[35].

**Development of RVE with ASR induced cracks**

**RVE of concrete as heterogeneous material**: Elastic properties of ASR affected concrete is numerically modelled using the proposed computational homogenization approach. Concrete at the mesoscale level consists of aggregates and cement paste. Before ASR occurrence, the volume fraction and properties of aggregates and cement paste determine the stiffness of the RVE[36]. Literature shows that the shape of aggregates has little effect on the elastic behaviour[37]. In the RVE model, the aggregates are considered to be circular and their diameters vary between 9.5mm and 19.5mm. The aggregate distribution curve shown in **Fig. 8 a** is based on Sanchez[5]. In the RVE model shown in **Fig. 8 b**, we have used maximum possible aggregate sizes passing through the sieve opening, i.e. the number of aggregates corresponding to diameters of 9.5mm, 12.7mm, 16.0mm and 19.5mm are 4, 5, 5 and 2, respectively. The aggregate distribution curve in **Fig. 8 a** is somewhat standard and the use of similar dimensions and volume fractions can be found in the literature, e.g. Wriggers and Moftah[36], Kim and Al-Rub[37]. Properties of the aggregate and cement and the corresponding volume fraction used in the RVE model are shown in **Table 1.** As discussed by Mirkhalaf et al.[38] and Rezakhani et al.[39], the size of RVE is selected based on the maximum aggregate size, where 75 x 75 $mm^2$ RVE size is deemed accurate. The number of 4-node square elements used is 3600, which is small enough to keep the computational cost reasonably low. Lines of discontinuity due to phase changes (from aggregate to cement paste) are introduced using the Extended Finite Element Method, while keeping the underlying mesh regular[40]. As the bond between aggregate particles and cement paste is assumed to be perfect, very large interface cohesive stiffness values are used to represent the bond in Eq. (38).

**Procedure of introducing cracks into RVE**: The RVE of ASR affected concrete is modelled for three levels of expansion (i.e. 0.05%, 0.12% and 0.2%). The locations and sizes of ASR induced open cracks follow the qualitative damage model proposed by Sanchez et al[23]. Crack densities corresponding to expansion levels given in **Fig. 7b** for different concrete mixtures have been averaged and used to calculate the crack lengths and numbers in the RVE.

By taking the average length of an open crack in a 1 $cm^2$ cell as 0.707 cm, the crack density data from **Fig. 7b** is converted to total crack length in the RVE. Based on the quantitative information for a given level of expansion, the shapes and locations of the cracks in the RVE are determined. These calculations are displayed in **Table2**, which were used as the input data for the RVE model as shown in **Fig. 9.** Typical cracked aggregate particles at different expansion levels are also presented in **Fig. 9.** It is worth noting herein that cracks networks observed in experimental testing are far more connected as both close and open cracks are measured, while in the numerical model, only open cracks were considered. Since the majority of the ASR induced cracks occur within the aggregate [22, 23], 75% of the open cracks are placed in the aggregate particles present in the RVE model. Open cracks are again introduced into the RVE model by using the Extended Finite Element Method[34]. ASR induced cracks are assumed completely open and therefore, the interface cohesive stiffness in Eq. (38) is assumed as zero. The crack pattern used in the model meets both the qualitative and quantitative criteria of the ASR induced crack development as per Sanchez et al.[22, 23]. It should be noted that the stiffness of the aggregates and cement paste are assumed to remain the same at different levels of expansion and thus, the change in the effective properties of the macro-scale concrete is only due to development of open cracks at the meso-scale.

**Results and discussion**

The results of the RVE modelling are shown in Table 3 and plotted against the experimental data in **Fig. 10**, from which one can verify that the stiffness properties are close in both directions, i.e., $\hat{D}_{1111} \approx \hat{D}_{2222}$. Numerical predictions of $\hat{D}_{1111}$ and $\hat{D}_{2222}$ based on the RVE always fall in between upper and lower bounds based on the experimental data of Sanchez et al.[35] . This outcome encourages the use of crack development patterns and density information proposed by Sanchez[23]. It is worth noting that the experimental data averaged in **Table 3** is collected from five 35MPa concrete mixtures whose modulus of elasticity vary between 30GPa and 38GPa. **Fig.10** shows that the stiffness reduction based on RVE remains in between the experimental results based on those 5 mixtures and thus, the RVE results are fully within the range of the experimental data. The aggregate distribution and material properties were assumed within a reasonable range because of the lack of detailed information. However, it is shown in **Figs. 11-16** that variations from the assumed values cause insignificant differences in terms of the predicted stiffness reductions in elastic modulus due ASR. **Figs. 11** and **12** show the reductions in $\hat{D}_{1111}$ and $\hat{D}_{2222}$, respectively of the RVE model for different expansion levels when the elasticity modulus of the concrete is varied between 18GPa and 22GPa. **Fig. 13** shows that the reduction percentage is not affected by the concrete grade. Similarly, **Figs. 14** and **15** show the reductions in $\hat{D}_{1111}$ and $\hat{D}_{2222}$ when the elasticity modulus of the aggregate is varied between 54GPa and 67GPa. Again, the reduction percentages in the stiffnesses corresponding to different expansion values are not affected as shown in **Fig. 16**. On the other hand, in predicting the stiffness values, current study assumes stationary cracks and does not consider the friction between rough surfaces of slightly open cracks. Consideration of friction and contact could be particularly important in predicting the strength and progressing crack propagations. In such a progressive failure analysis assumption of Periodic RVE boundary conditions may become less accurate especially when the cracks hit the boundaries. Several strategies have been proposed to predict the RVE boundary conditions when periodicity assumption due to crack propagation needs to be abandoned e.g., Larsson et al.[32]

## FURTHER RESEARCH

Based on the insight gained in this study, the meso-scale RVE based computational homogenization procedure can be extended to a wider range of concrete mixtures presenting distinct aggregate natures and reactivities (i.e. potential to reach different and higher expansion levels). Uncertainties in the stiffness properties, aggregate volume fractions and the crack pattern can be accounted for by utilizing stochastic approaches. The proposed crack development scheme can be used as a basis in model updating strategies for damage detection purposes. For residual load capacity predictions of ASR affected structures, meso-scale RVE modelling approach can be adopted within a two-scale structural analysis frame-work.

## CONCLUSIONS

A computational homogenization procedure was developed to determine the effective stiffness of ASR-affected concrete mixtures. The meso-scale RVE model was continuum-based in which circular aggregates and cement matrix were assumed fully bonded in the concrete mix. ASR induced cracks were considered fully open, i.e., cohesionless and frictionless. Discontinuities (due to phase changes and/or crack openings) were efficiently introduced into the regularly meshed RVE model by using the Extended Finite Element Method. For 35 MPa concrete mixtures incorporating reactive coarse aggregates, the results suggest that up to 0.2% ASR induced expansion levels, about 75% of the cracks develop within the aggregate particles. While the experimental results used for benchmarking purposes showed variations, in all cases considered in the current study they provided upper and lower bounds to the proposed meso-scale RVE model results. In this intricate problem of solid mechanics with inherent uncertainties, and considering the lack of accurate predictive tools, the outcomes encourage the use of proposed crack development patterns and density information for modelling purposes up to 0.2% ASR induced expansion levels.

## ACKNOWLEDGMENTS

The authors wish to express their gratitude and sincere appreciation to the Mitacs Globalink Research Award, the Australian Research Council Research Hub (IH150100006) for Nanoscience Based Construction Materials Manufacturing (NANOCOMM) and the industry partner Roads and Maritime Services (RMS) for financing this research.

## REFERENCES

1. Giaccio, G; Zerbino, R.; Ponce, J.M; and Batic, O.R., "Mechanical behavior of concretes damaged by alkali-silica reaction," *Cement and Concrete Research*, V. 38, 2008, No. 7, pp. 993-1004.

2. Multon, S.; Seignol, J.F., and Toutlemonde, F., "Structural behavior of concrete beams affected by alkali-silica reaction," *ACI Materials Journal*, V. 102, 2005, No. 2, pp. 67-76.

3. Swamy, R.N. and Al-Asali, M.M., "Engineering properties of concrete affected by alkali-silica reaction," *Materials Journal*, V. 85, 1988, No. 5, pp. 367-374.

4. Fournier, B.; Bérubé, A., "Alkali-aggregate reaction in concrete: a review of basic concepts and engineering implications", *Canadian Journal of Civil Engineering*, 27, 2000, No. 2, pp. 167-191.

5. Sanchez, L.F.M., "Contribution to the Assessment of Aging Concrete Infrastructures Affected by Alkali-Aggregate Reaction", PhD Thesis, Université Laval, 2014.

6. CSA A23.1., "Concrete Materials and Methods of Concrete Construction - APPENDIX B". Canadian Standards Association, Mississauga, Ontario (Canada), 2014.

7. ASTM C 1293. "Standard test method for determination of length change of concrete due to alkali-silica reaction". ASTM International, West Conshohocken (USA), 2012.

8. AASHTO, "Determining the Reactivity of Concrete Aggregates and Selecting Appropriate

Measures for Preventing Deleterious Expansion in New Concrete Construction: Final Report", FHWA & AASHTO ASR Task Group, 2010.

9. Folliard, K.J., Barborak, R., Drimalas, T., Du, L., Garber, S., Ideker, J., Ley, T., Williams, S., Juenger, M., Fournier, B., Thomas, M.D.A., "Preventing ASR/DEF in New Concrete: Final Report", Texas Department of Transportation (TxDOT), 2006.

10. Malvar, L.J., Cline, G.D., Burke, D.F., Rollings, R., Sherman, T., Greene J., "Alkali-Silica Reaction Mitigation: State-of-the-Art", Final Report, Naval Facilities Engineering Service Center, 2001.

11. Ballard, Zachoriah J., William S. Caires, and Stanley R. Peters, "Alternate Mitigation Materials for Alkali-Silica Reaction (ASR) in Concrete", No. CDOT-2008-10. Colorado Department of Transportation, DTD Applied Research and Innovation Branch, 2008.

12. Pietruszczak, S., "On the mechanical behaviour of concrete subject to Alkali Silica Reaction," *Computers & Structures*, V. 58, 1996, pp. 1093-1097.

13. Saouma, V.E., Numerical modelling of AAR; CRC Press, 2014.

14. Erkmen, R.E.; Gowripalan, N., and Sirivivatnanon, V., "Elasto-plastic damage modelling of beams and columns with mechanical degradation," *Computers and Concrete*, V. 19, 2017, pp. 315-323.

15. Gorga, R.; Sanchez, L., and Martin-Perez, B. "FE approach to perform the condition assessment of a concrete overpassed damaged by ASR after 50 years in service," *Engineering Structures*, V. 177, 2018, pp. 133-146.

16. Reinhardt, H.W., and Mielich, O., "A fracture mechanics approach to the crack formation in alkali-sensitive grains," *Cement and Concrete Research*, V. 41, 2011, No. 3, pp. 255-262.

17. Multon, S.; Sellier, A., and Cyr, M., "Chemo–mechanical modeling for prediction of alkali silica reaction (ASR) expansion," *Cement and Concrete Research*, V. 39, 2009, pp.490–500.

18. Poyet, S.; Sellier, A.; Capra, B.; Foray, G.; Torrenti, J.M.; Cognon, H., and Bourdarot, E.,

"Chemical modelling of alkali silica reaction: influence of the reactive aggregate size distribution," *Materials and Structures*, V. 40, 2007, No. 2, pp. 229-239.

19. Suwito, A.; Jin, W.; Xi, Y., and Meyer, C., "A mathematical model for the pessimum effect of ASR in concrete," *Concrete Science and Engineering*, V. 4, 2002, pp. 23–34.

20. Nielsen, A.; Gottfredsen, F., and Thogersen, F., "Development of stresses in concrete structures with alkali–silica reactions," *Materials and Structures*, V. 26, 1993, pp.152–8.

21. Dunant, C.F., and Scrivener, K.L., "Micro-mechanical modelling of alkali-silica reaction induced degradation using AMIE framework," *Cement and Concrete Research,* V. 40, 2010, pp. 517-525.

22. Sanchez, L. F. M.; Fournier, B.; Jolin, M.; Bedoya, M. A. B.; Bastien, J., and Duchesne, J., "Use of Damage Rating Index to Quantify Alkali-Silica Reaction Damage in Concrete: Fine versus Coarse Aggregate," *ACI Materials Journal*, V. 113, 2016, No. 4, pp. 395–407.

23. Sanchez, L. F. M.; Fournier, B.; Jolin, M., and Duchesne, J., "Reliable quantification of AAR damage through assessment of the Damage Rating Index (DRI), "*Cement and Concrete Research,*" V. 67, 2015, pp. 74-92.

24. Comby-Peyrot, I.; Bernard, F.; Bouchard, P.O.; Bay, F., and Garcia-Diaz, E., "Development and validation of a 3D computational tool to describe concrete behaviour at mesoscale. Application to the alkali-silica reaction," *Computational Material Science*, V. 46, 2009, pp. 1163-1177.

25. Cusatis, G.; Di Luzio, G., and Cedolin, L., "Meso-scale simulation of concrete: Blast and Penetration affects and AAR degradation," *Applied Mechanics and Materials*, V. 82, 2011, pp. 75-80.

26. Ishakov, T.; Timothy, J.T., and Meschke, G., "Expansion and deterioration of Concrete due to ASR: Mechanical Modelling and Analysis," *Cement and Concrete Research*, V.115, 2019, pp. 507-518.

27. Rezaghani, R., Alnaggar, M., and Cusatis, G., "Multiscale homogenization analysis of Alkali-Silica Reaction (ASR) Effect in Concrete," *Engineering*, 2019.

28. Holmes, M.H. Introduction to Perturbation Methods, 2013, 2nd edition, Springer.

29. Kanit, T.; Forest, S.; Galliet, I.; Mounoury, V., and Jeulin, D., "Determination of the size of the representative volume element for random composites: statistical and numerical approach," *International Journal of Solids and Structures*, V. 40, 2003, pp. 3647-3679.

30. Miehe, C., and Koch, A., "Computational micro-macro transitions of discretised microstructures undergoing small strains," *Archieves of Applied Mechanics*, V. 72, 2002, pp. 300-317.

31. Belytschko, T.; Liu, W.K.; Moran, B., and Elkhodary, K., Nonlinear Finite Elements for Continua and Structures, 2014, Wiley & Sons.

32. Larsson, F.; Runesson, K.; Saroukhani, S., and Vafadari, R., "Computational homogenization based on a weak format of micro-periodicity for -problems," *Computer Methods in Applied Mechanics and Engineering*, V. 200, 2011, pp. 11-26.

33. Melenk, J.M., and Babuška, I., "The partition of unity finite element method: Basic theory and applications," *Computer Methods in Applied Mechanics and Engineering*, V. 139, 1996, pp. 289-314.

34. Belytschko, T., and Black, N., "Elastic crack growth in finite elements with minimal remeshing," *International Journal for Numerical Methods in Engineering*, V.45, 1999, pp. 601-620.

35. Sanchez, L. F. M.; Fournier, B.; Jolin, M.; Mitchell, D., and Bastien, J., "Overall assessment of Alkali-Aggregate Reaction (AAR) in concretes presenting different strengths and incorporating a wide range of reactive aggregate types and natures," *Cement and Concrete Research*, V.93, 2017, pp. 17-31.

36. Wriggers, P., and Moftah, S.O., "Mesoscale models for concrete: Homogenisation and

damage behavior," *Finite Elements in Analysis and Design*, V. 42, 2006, No. 7, pp.623-636.

37. Kim, S. M., and Al-Rub, R. K. A., "Meso-scale computational modeling of the plastic-damage response of cementitious composites," *Cement and Concrete Research*, V. 41, 2011, No.3, pp. 339-358.

38. Mirkhalaf, S. M.; Pires, F. A., and Simoes, R., "Determination of the size of the Representative Volume Element for the simulation of heterogeneous polymers at finite strains," *Finite Elements in Analysis and Design*, V.119, 2016, pp. 30-44.

39. Rezakhani, R.; Zhou, X., and Cusatis, G., "Adaptive multiscale homogenization of the lattice discrete particle model for the analysis of damage and fracture in concrete," *International Journal of Solids and Structures*, V.125, 2017, pp.50-67.

40. Sukumar, N.; Chopp, D.L.; Moes, N., and Belytschko, T. C., "Modeling voids and inclusions by level sets in extended finite element method," *Computer Methods in Applied Mechanics and Engineering*, V. 190, 2001, pp. 6183-6200.

## TABLES AND FIGURES

**List of Tables:**



**List of Figures:**

**Fig. 6 –** Crack development due to ASR: (a) Open cracked in aggregate and cement paste; (b) Qualitative damage model at different levels of expansion [adapted from Sanchez et al (2015)]

**Fig. 7 –** Modulus of elasticity reduction (a) and crack density (b) as function of expansion degree [Adapted from Sanchez (2017)]

**Fig. 8** – (a) Aggregate size distribution curve (b) Geometry of the RVE used in this study

**Fig. 9 –** RVE of concrete at different levels of expansion and typical development of cracks in a single aggregate in the RVE

**Fig. 10 –** The reduction of concrete stiffness vs. expansion based on the homogenized RVE

**Table 1 –** Material properties used in the RVE

| Parameter | Value |
|---|---|
| Young's modulus of cement | 20 GPa |
| Poisson's ratio of cement | 0.2 |
| Young's modulus of aggregates | 60 GPa |
| Poisson's ratio of aggregates | 0.2 |
| Aggregate sizes | 9.5-19.5 mm |
| Volume fraction of aggregates | 45 % |

**Table 2 –** Information on open cracks in the RVE of ASR affected concrete

| Expansion level | Crack density (counts/cm$^2$) | Total number of cracks per RVE (75x75 mm$^2$) | Total length (mm) | Total length of crack in aggregate (mm) | Total length of crack in cement (mm) |
|---|---|---|---|---|---|
| 0.05% | 0.9 | 50.6 | 358.0 | 268.5 | 89.5 |
| 0.12% | 1.4 | 78.8 | 556.8 | 417.6 | 139.2 |
| 0.20% | 2.2 | 123.8 | 875.0 | 656.3 | 218.8 |

**Table 3** – Effective stiffness properties of ASR affected concrete in GPa

| Expansion Level | RVE $\hat{D}_{1111}$ **(reduction)** | RVE $\hat{D}_{1122}$ | RVE $\hat{D}_{1112}$ | RVE $\hat{D}_{2222}$ **(reduction)** | RVE $\hat{D}_{2212}$ | RVE $\hat{D}_{1212}$ | Experiment [Sanchez[35]] **(reduction)** |
|---|---|---|---|---|---|---|---|
| 0.00% | 33.6 **(0.00%)** | 8.3 | 0.05 | 33.8 **(0.00%)** | -0.12 | 12.3 | 30 – 38 |
| 0.05% | 29.2 **(13.1%)** | 6.52 | -0.04 | 29.7 **(12.1%)** | -0.2 | 11.3 | **(16.1%)** |
| 0.12% | 24.1 **(28.3%)** | 4.69 | 0.03 | 24.8 **(26.6%)** | -0.01 | 9.93 | **(33.6%)** |
| 0.20% | 18.8 **(44.0%)** | 2.65 | 0.13 | 18.6 **(45.0%)** | 0.28 | 8.13 | **(41.1%)** |

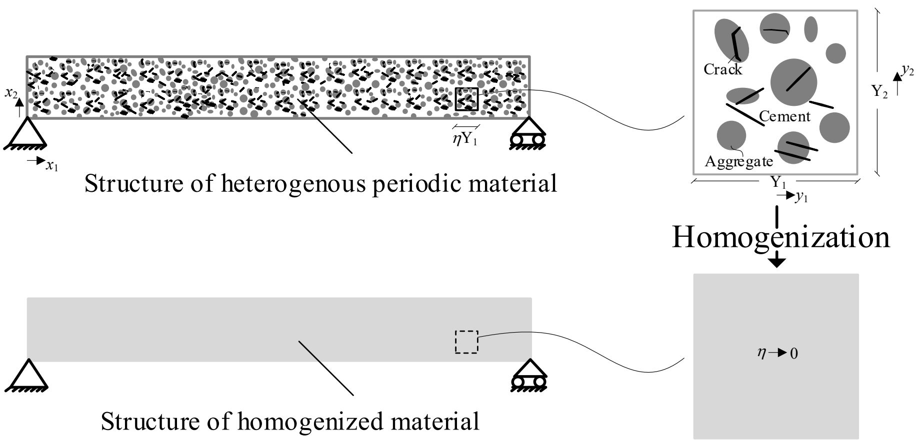


***Fig. 1*** *– Schematic description of scale separation*

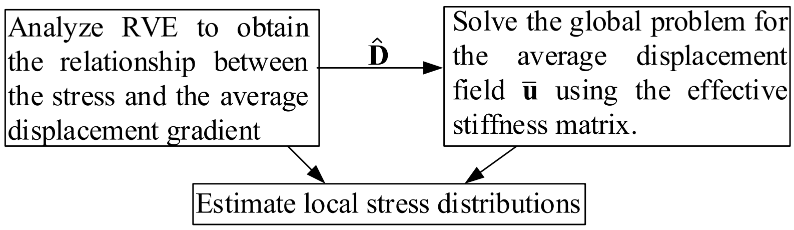


***Fig. 2*** *– Schematic outline for the two-scale analysis procedure*

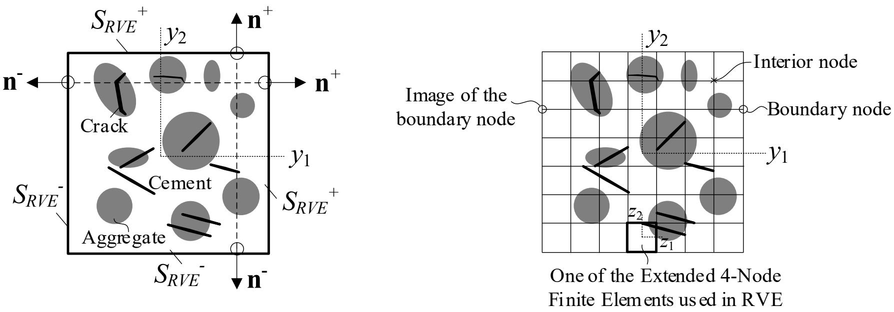


a) Schematic picture b) Mesh for the numerical solution

***Fig. 3** – RVE of cracked concrete*

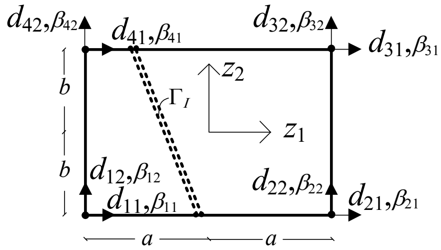


***Fig. 4** – Standard bilinear rectangular element enriched to introduce discontinuity*

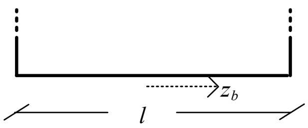


***Fig. 5** – Edge of the Element*

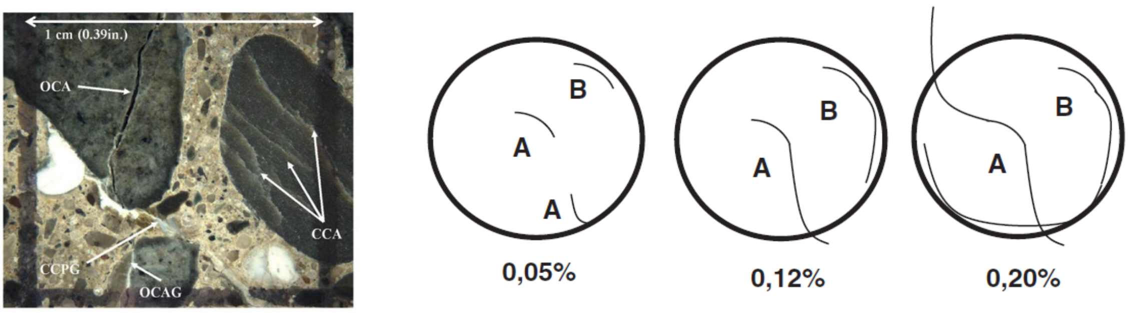


(a) (b)

***Fig. 6** – Crack development due to ASR: (a) Open cracked in aggregate and cement paste;*

*(b) Qualitative crack development model at different levels of expansion* [based on Sanchez[23]]

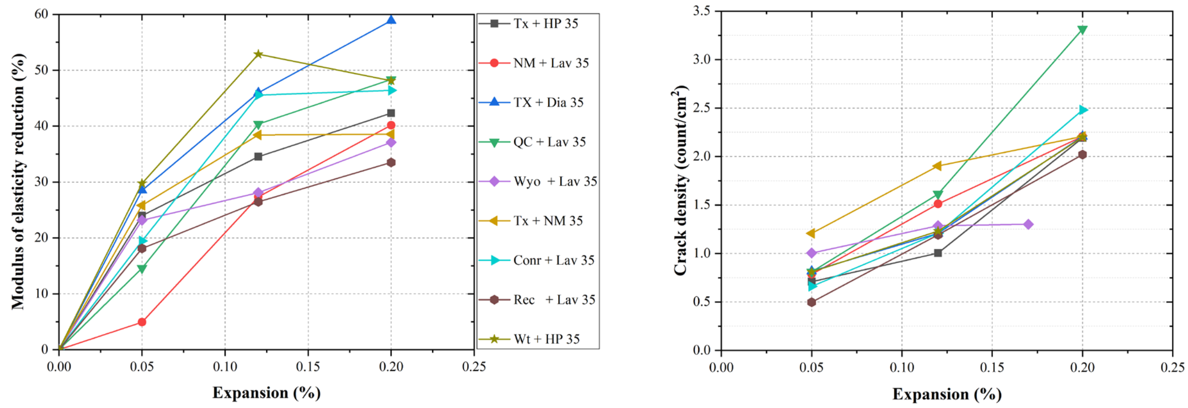


(a) (b)

***Fig.** 7 – Modulus of elasticity reduction (a) and crack density (b) as function of expansion degree [based on Sanchez[35]]*

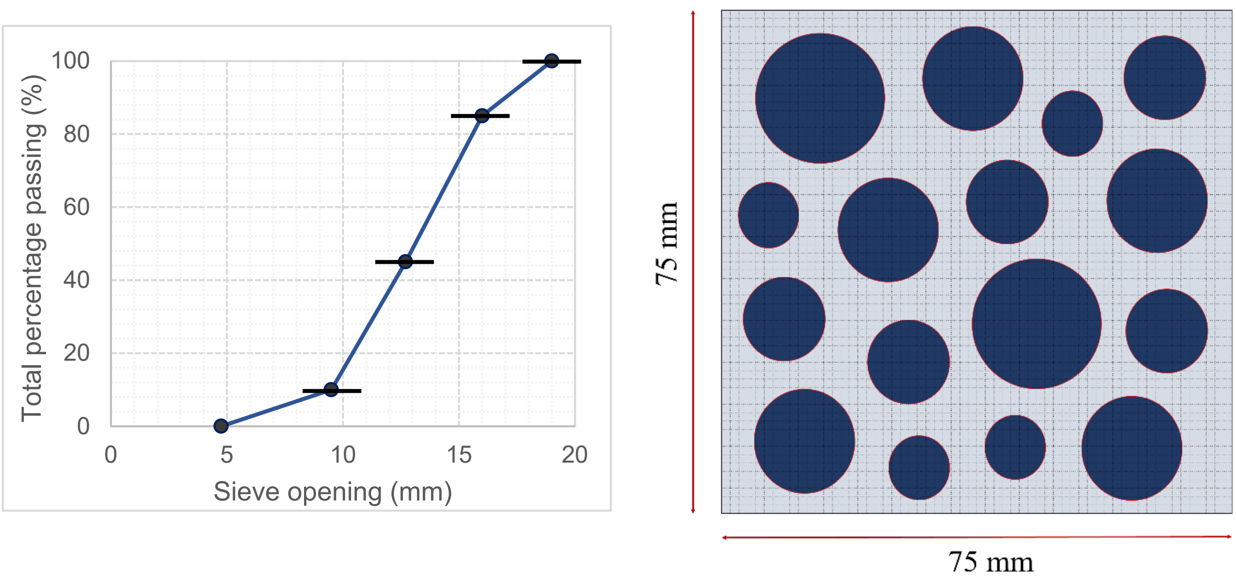


(a) (b)

***Fig. 8** –(a) Aggregate size distribution curve considered in this study (b) geometry of the RVE*

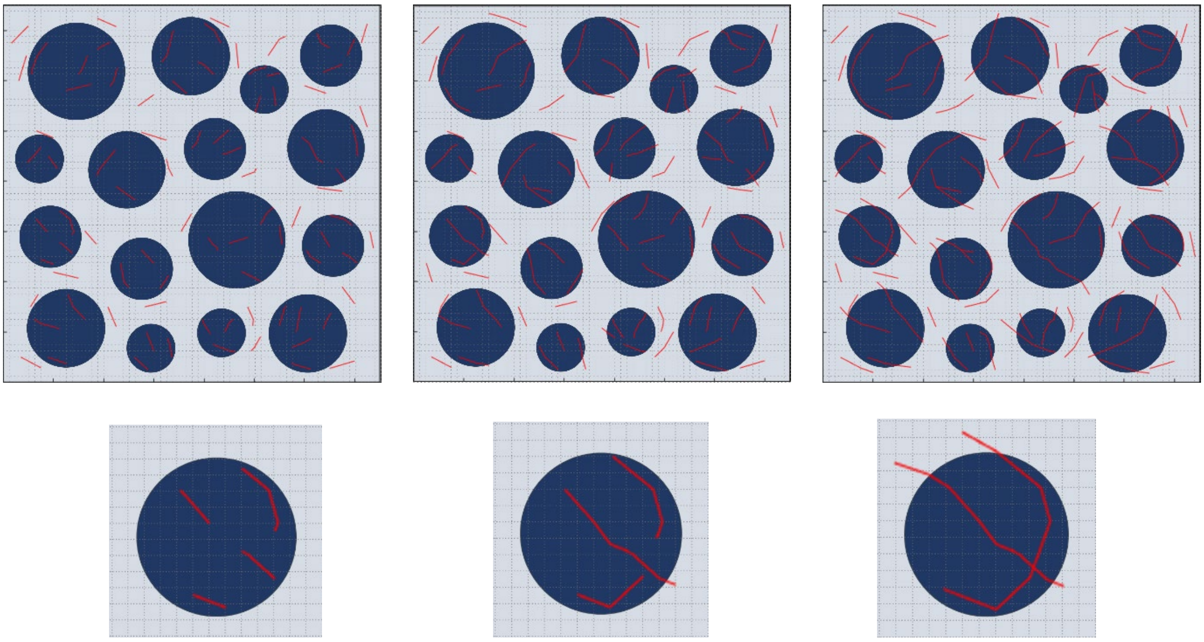

(a) 0.05 %　　(b) 0.12 %　　(c) 0.2 %

***Fig. 9*** *– RVE of concrete at different levels of expansion and typical development of cracks in a single aggregate in the RVE*

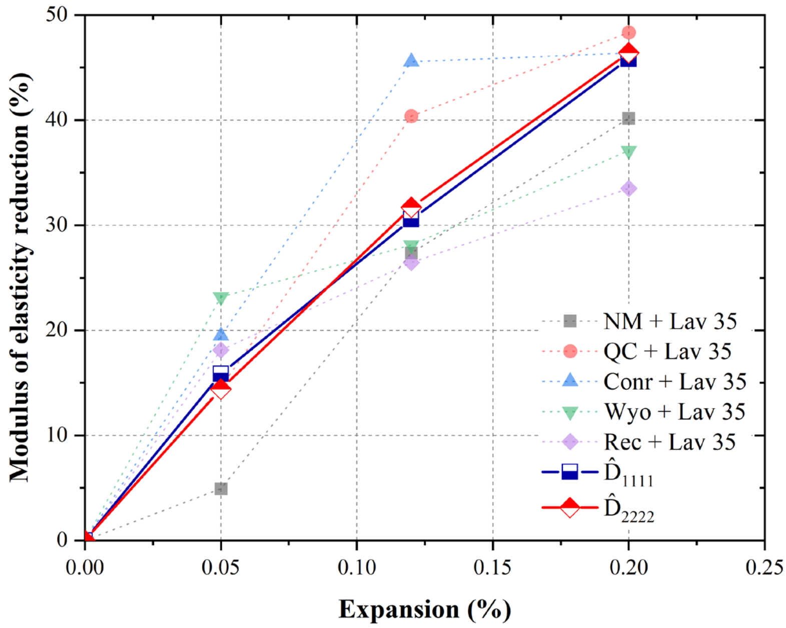


***Fig. 10*** *– Reduction of concrete stiffness vs. expansion based on the homogenized RVE*

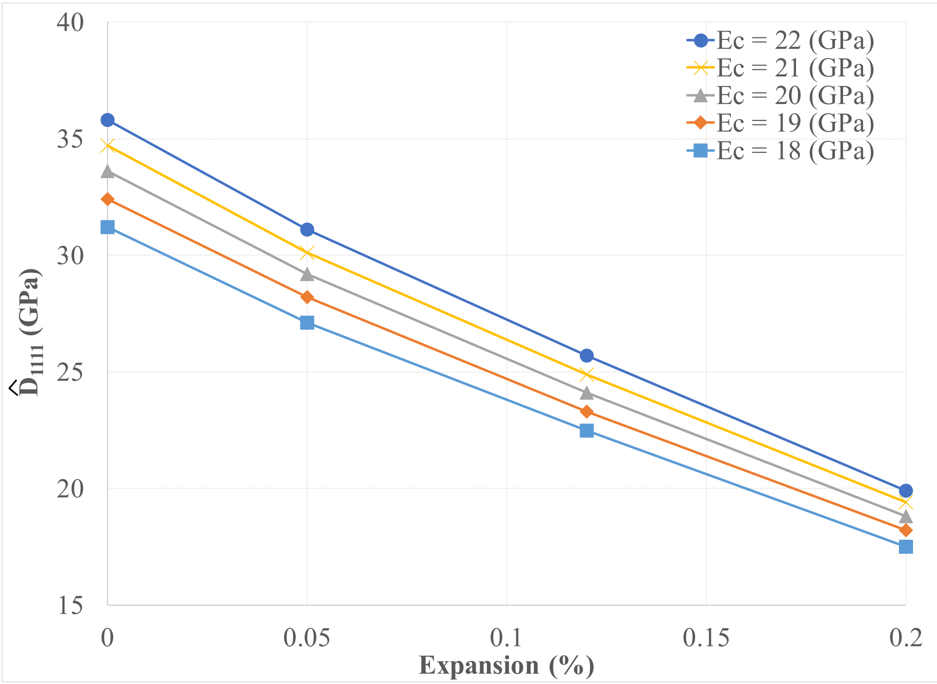


***Fig. 11*** *– Reduction in* $\hat{D}_{1111}$ *vs. expansion for different Cement Elastic Moduli*

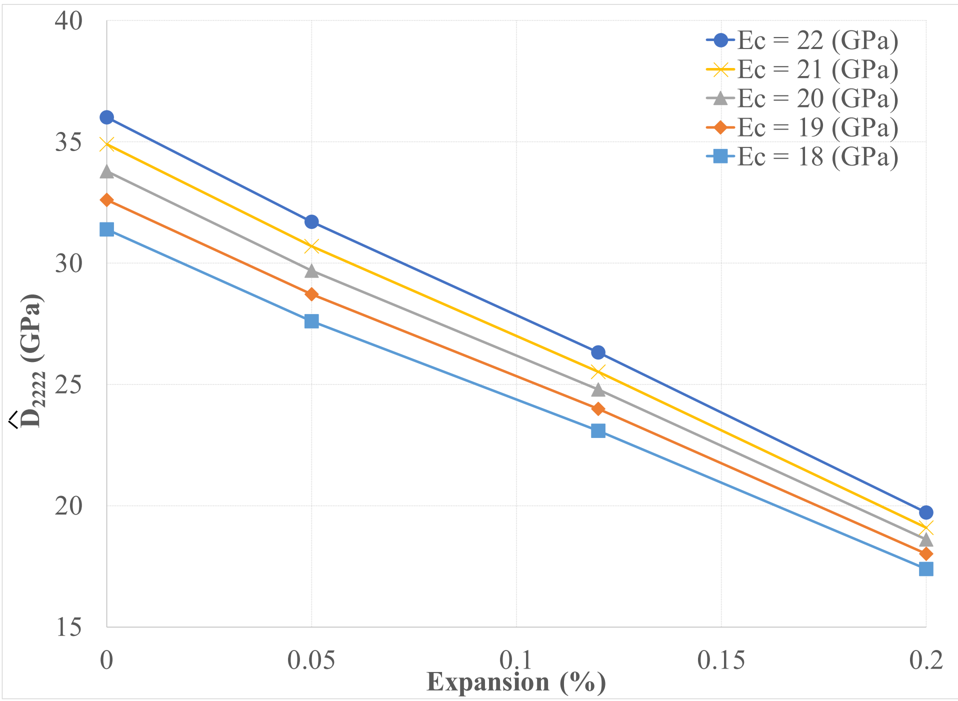


***Fig. 12*** *– Reduction in* $\hat{D}_{2222}$ *vs. expansion for different Cement Elastic Moduli*

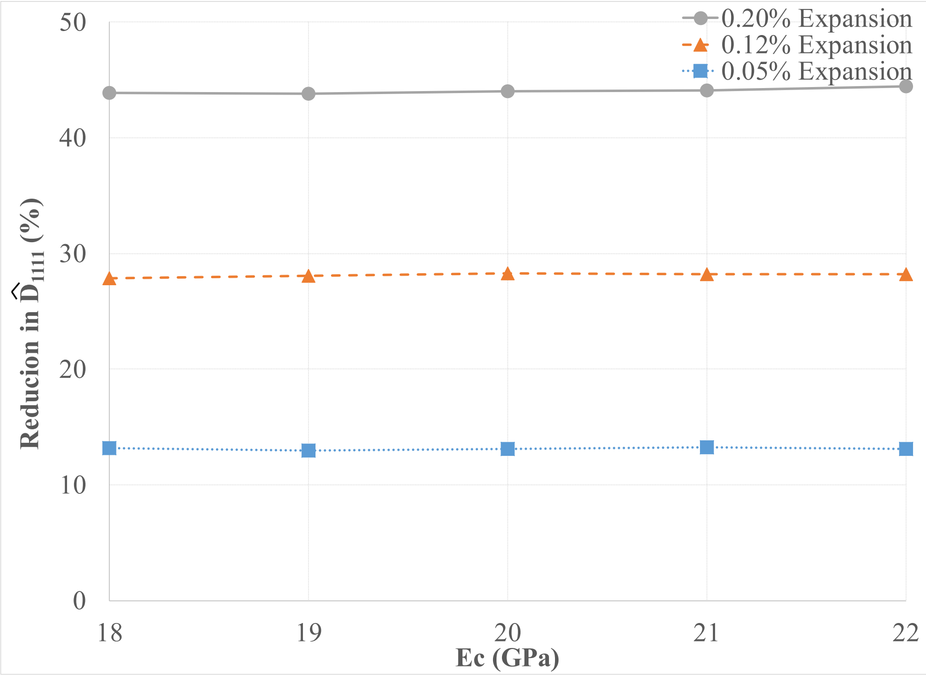


***Fig. 13*** *– Effect of Cement Elastic Modulus on ASR related reduction of concrete stiffness*

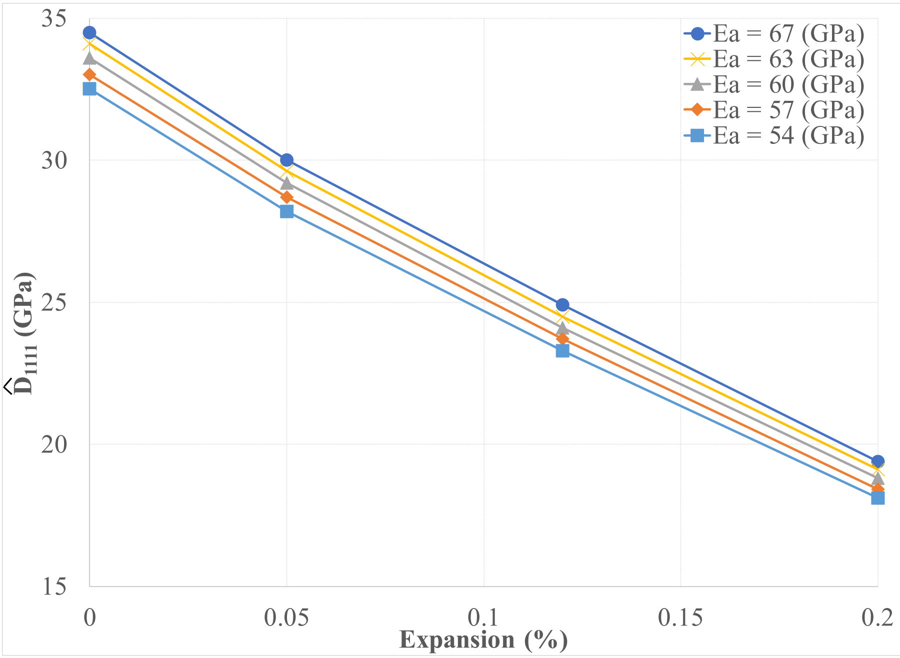


***Fig. 14*** *– Reduction in* $\hat{D}_{1111}$ *vs. expansion for different Aggregate Elastic Moduli*

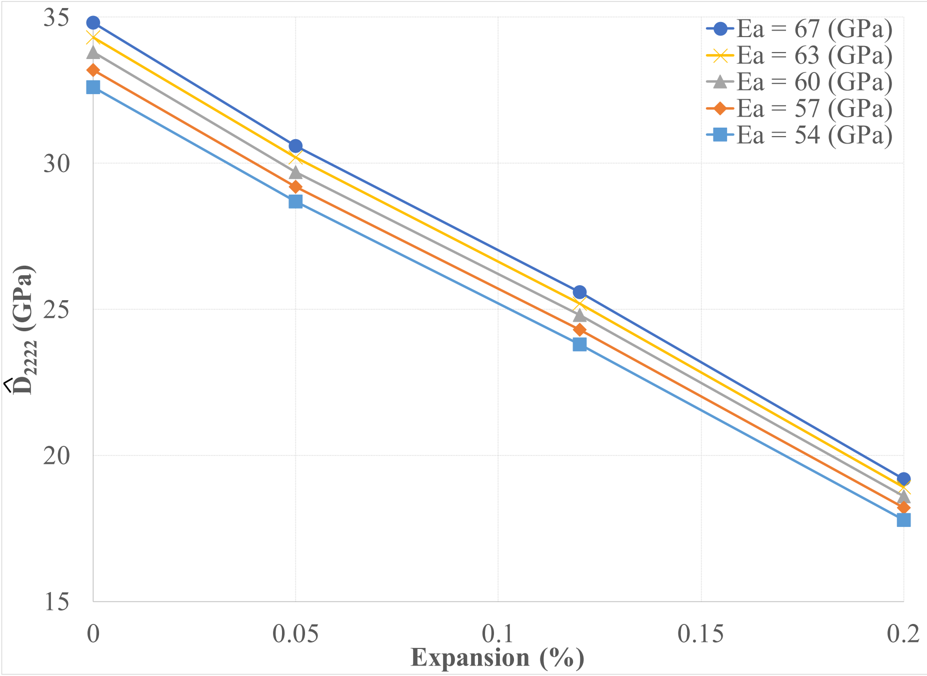


***Fig. 15*** *– Reduction in* $\hat{D}_{2222}$ *vs. expansion for different Aggregate Elastic Moduli*

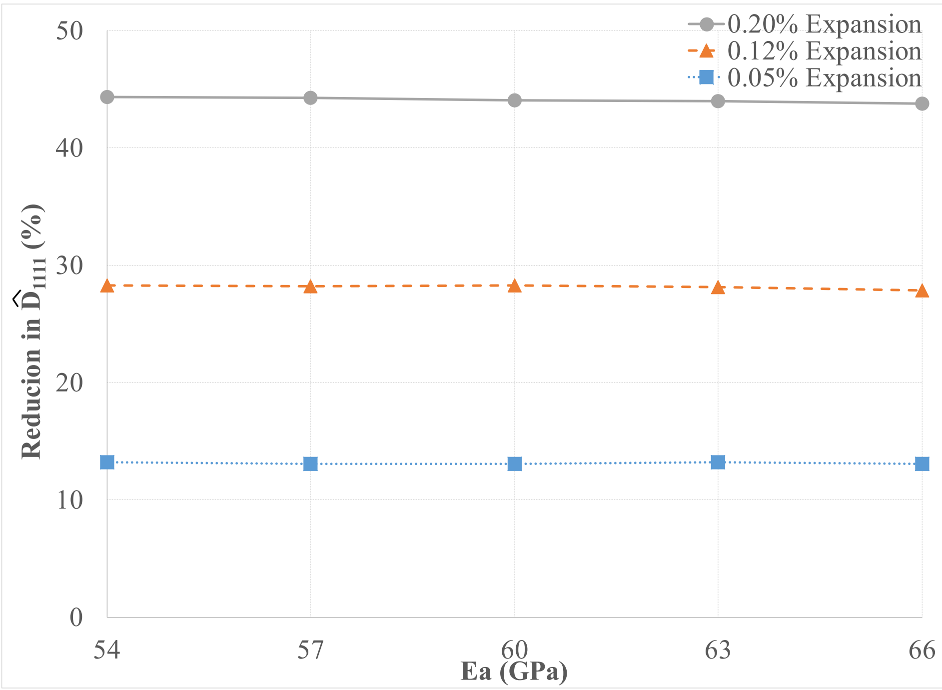


***Fig. 16*** *– Effect of Aggregate Elastic Modulus on ASR related reduction of concrete stiffness*